PASJ: Publ. Astron. Soc. Japan **62**, 879–891, 2010 August 25

Internal Fine Structure of Ellerman Bombs

Yuki HASHIMOTO,[1,2] Reizaburo KITAI,[2,3] Kiyoshi ICHIMOTO,[2] Satoru UENO,[2] Shin'ichi NAGATA,[2]
Takako T. ISHII,[2] Masaoki HAGINO,[4] Hiroyuki KOMORI,[2] Keisuke NISHIDA,[1,2] Takuma MATSUMOTO,[1,2]
Kenichi OTSUJI,[1,2] Tahei NAKAMURA,[1,2] Tomoko KAWATE,[1,2] Hiroko WATANABE,[1,2] and Kazunari SHIBATA[2,3]
[1]*Department of Astronomy, Kyoto University, Kitashirakawa-Oiwake-cho, Sakyo-ku, Kyoto 606-8502*
hasimoto@kwasan.kyoto-u.ac.jp
[2]*Kwasan and Hida Observatories, Kyoto University, Yamashina-ku, Kyoto 607-8471*
[3]*Unit of Synergetic Studies for Space, Kyoto University, Yamashina-ku, Kyoto 607-8471*
[4]*National Astronomical Observatory, 2-21-1 Osawa, Mitaka, Tokyo 181-8588*

(Received 2009 June 30; accepted 2009 November 24)

Abstract

We conducted coordinated observations of Ellerman bombs (EBs) between Hinode Satellite and Hida Observatory (HOP12). Ca II H broad-band filter images of NOAA 10966 on 2007 August 9 and 10 were obtained with the Solar Optical Telescope (SOT) aboard the Hinode Satellite, and many bright points were observed. We identified a total of 4 bright points as EBs, and studied the temporal variation of their morphological fine structures and spectroscopic characteristics. With high-resolution Ca II H images of SOT, we found that the EBs, thus far thought of as single bright features, are composed of a few of fine subcomponents. Also, by using Stokes I/V filtergrams with Hinode/SOT, and Ca II H spectroheliograms with Hida/Domeless Solar Telescope (DST), our observation showed: (1) The mean duration, the mean width, the mean length, and the mean aspect ratio of the subcomponents were 390 s, 170 km, 450 km, and 2.7, respectively. (2) Subcomponents started to appear on the magnetic neutral lines, and extended their lengths from the original locations. (3) When the Ca II H line of EBs showed the characteristic blue asymmetry, they are associated with the appearance or re-brightening of subcomponents. Summarizing our results, we obtained an observational view that elementary magnetic reconnections take place one by one successively and intermittently in EBs, and that their manifestation is the fine subcomponents of the EB phenomena.

Key words: Sun: chromosphere — Sun: Ellerman bombs — Sun: magnetic fields — Sun: photosphere

1. Introduction

Ellerman bombs (EBs: Ellerman 1917) are known to be chromospheric phenomena. EBs have broad emission with central absorption in Hα spectra, and sometimes are referred to as moustaches owing to their spectral appearance. The typical size of EBs is on the order of $1''$, and the typical lifetime is 10–20 min (Roy & Leparskas 1973; Kurokawa et al. 1982; Zachariadis et al. 1987; Nindos & Zirin 1998; Qiu et al. 2000; Georgoulis et al. 2002).

Several explanations for the characteristic line profile of EBs have been proposed. Kitai (1983) reproduced the Hα profile by non-LTE calculations of a perturbed, heated, and condensed chromosphere. Firstova (1986) has detected linear polarization in the moustaches of Hα and Hβ lines, and concluded that the linear polarization of the moustache lines is likely to be reproduced by an energetic particle beam. Ding, Hénoux, and Fang (1998) and Hénoux, Fang, and Ding (1998) also considered the heated atmosphere by energetic particle beams, and reproduced line profiles of EBs.

Pariat et al. (2004) suggested that EBs are linked by a hierarchy of elongated flux tubes showing aperiodic spatial undulations. Flux tubes in the subphotosphere emerge undulatory by Parker instability (Parker 1966), and EBs occur as a result of magnetic reconnection at the dipped lower parts. Matsumoto et al. (2008a) found the association of bi-directional flows at the locations of EBs, and argued that the bi-directional flows are supportive evidence of magnetic reconnection. Isobe et al. (2007) supported resistive flux emergence models with a two-dimensional MHD simulation. With the Hinode images, Matsumoto et al. (2008b) analyzed the internal structure of EBs, and found that an EB is composed of a central elongated bright core located along the magnetic neutral line and a diffuse halo. Based on the observed internal structure, he proposed a more elaborate reconnection model of EBs, in which the elliptical bright core corresponds to the heated-up gas by reconnection. Watanabe et al. (2008) reported the undulatory pattern in the horizontal components of the magnetic field, and confirmed the association between EBs and emerging flux tubes. All of these observational studies support the magnetic reconnection model to trigger the EBs.

Although many studies of EBs have been conducted, and several models for EBs have been proposed, details of the triggering mechanism and the temporal evolution of EBs has not yet been clearly understood. To advance our understanding of EB physics, we conducted coordinated observations between Hinode Satellite and Hida Observatory (HOP12). We obtained spatially high resolution images of EBs with Hinode/Solar Optical Telescope (SOT: Ichimoto et al. 2004; Shimizu et al. 2008; Suematsu et al. 2008; Tsuneta et al. 2008), while we obtained highly resolved Ca II H spectra of EBs with Domeless Solar Telescope (DST: Nakai & Hattori 1985). We were successful in following the temporal evolution of 4 EBs, both in imagery and in spectra. Our analysis concentrated on:

(1) the fine structure of EBs, their lifetimes and morphological shapes, (2) the correlation between the location of the EBs and the distribution of the photospheric magnetic field, and (3) the temporal variation of the Ca II H spectrum. We obtained an observational view that elementary magnetic reconnections take place one by one successively and intermittently in EBs, and that their manifestation is the fine subcomponents of the EB phenomena.

2. Observation

Figure 1 and figure 2 show the active region of NOAA 10966 on 2007 August 9 and 10 observed with Hinode/SOT and Hida/DST. The active region was located at S05, W05 on the disk. Many Ca II H bright points appear in the active region. Among them, we picked up bright points indicated by A, B, C, and D. These bright points did not appear in the Hα center image, while they appeared bright in Hα wing images. As will be shown in a later section, the Ca II H spectra of these points showed characteristic moustache shapes. Therefore, we identified these bright points as being EBs.

With Hinode/SOT, Ca II H (3968.5 Å) filtergrams of the region were taken through the Broad band Filter Imager (BFI) with a pass-band of 3 Å, with a diffraction of 50 cm aperture. The spatial resolutions were $0.''11$ pixel^{-1} and the cadence was 45 s. Stokes I/V filtergrams of the region were also observed. Stokes I/V filtergrams were reduced from Fe I (6302 Å) shutterless filtergrams. We only used the ratio of Stokes I/V as a proxy for magnetograms, because the inversion to the magnetic field with one wavelength polarimetric data is not fully established at present. The images were taken through the Narrow band Filter Imager (NFI) with a pass-band of 90 mÅ. The spatial resolutions were $0.''16$ pixel^{-1} and the cadence was 45 s.

With Hida/DST, we obtained the Hα center, ± 0.5 Å, ± 0.8 Å filtergrams using a tunable Lyot filter of 0.25 Å passband. The cadence of the Hα filtergram observation was nearly 15 s for each wavelength, and the spatial resolution of the filtergrams was around $1''$. We also obtained spectrograms of Ca II H with DST. The observed field of view (FOV), $120'' \times 128''$, was scanned with a slit of $128''$ length and of $0.''64$ width combining the spectrograms over the FOV; we constructed spectroheliograms in any specified wavelengths, a posteriori. The spatial scan step of the spectroscopic observation was $0.''48$. The cadence to scan over the FOV was nearly 15 s.

As we conducted coordinated observations between Hinode Satellite and Hida Observatory (HOP12), both Hinode/SOT and Hida/DST data were obtained during the same time span and covered the same target region.

3. Analysis

As mentioned in the introduction, for each EB, we studied (1) the fine structure seen in high-resolution images obtained by Hinode/SOT, (2) the correlation between the location of the EBs and the spatial distribution of the magnetic field, and (3) the temporal variation of the Ca II H spectrum. In this section, we show the methods of analyses for both Hinode/SOT and Hida/DST data.

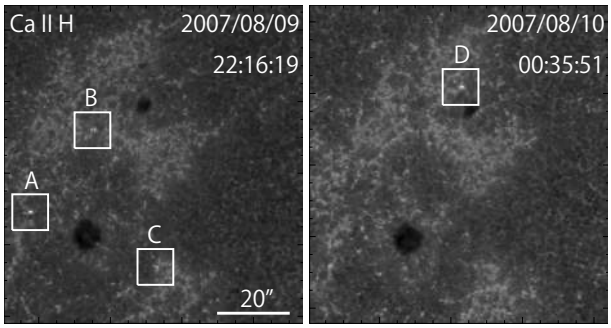

Fig. 1. Snapshot of NOAA 10966 in a Ca II H image of Hinode/SOT. The field of view was at S05, W05 on the disk. The EBs studied in this work are indicated by a square of $10''$ size.

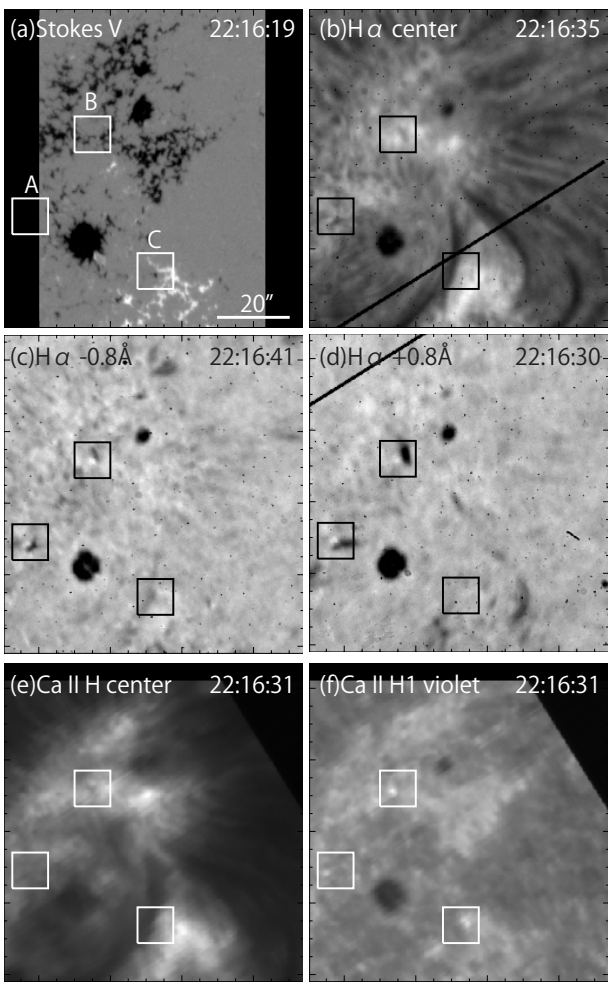

Fig. 2. Snapshot of NOAA 10966 at 22:16 UT on 2007 August 9. (a) Stokes V filtergrams of Hinode/SOT. (b–d) Filtergrams in Hα center, -0.8 Å, and $+0.8$ Å of Hida/DST. (e–f) Spectroheliograms in Ca II H center, and H_1 violet of Hida/DST, the times indicated in the panels correspond to the start time of the spatial scan. The EBs studied in this work are indicated by squares of $10''$ size. Each black line in (b), (d) shows the spectrograph slit.

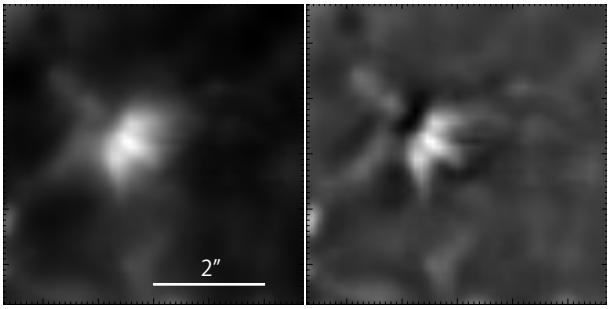

Fig. 3. Image enhancement by unsharp masking method. The left is the raw image observed in Ca II H with SOT and the right is the enhanced image of the raw data by the unsharp masking method. This example is EB(A).

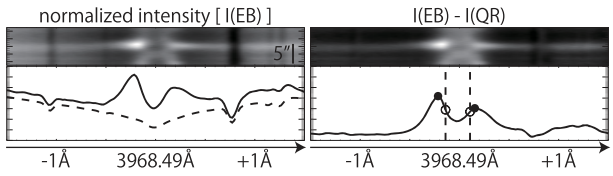

Fig. 4. Method of analyzing spectroheliograms of Ca II H with DST. The upper-left image shows the Ca II H spectrum of the EB. The lower-left panel is a profile of the Ca II H spectrum of the EB. The intensity was normalized. The dashed curve is the average profile of the quiet region used for a reference. The right image and the panel show the same as the left ones, but the intensity was shown by subtracting that of the quiet regions. Also, the lower-right panel shows the method of asymmetry. The white circles show the intensities at two wavelengths separated by ± 0.13 Å from the line center (vertical dashed lines), used to derive the asymmetry by the first method. The black circles show the wavelength locations of the peak intensities used to derive the asymmetry by the second method. This example is EB(A).

3.1. Hinode/SOT

For analyzing Ca II H filtergrams of SOT, dark subtraction and flat-fieldings were applied in a standard manner. To closely examine the fine structure of EBs, we applied the unsharp masking image (Malin 1977) processing method to the observed data, by the ssw_idl routine unsharp_mask.pro originally coded by A. McAllister and K. Strong (1992). The image was smoothed with a Gaussian filter of 1.″1 width. Subtraction of the smoothed image from the original one gave us a contrast-enhanced image of the fine features. Figure 3 shows an EB observed in Ca II H with SOT. The left is a raw image, and the right is the enhanced one by the unsharp masking method. We can see very fine internal features of the EB thus far undetected. As can be seen in figure 3, dark features are also enhanced around the bright area. This is an artifact and a drawback of this method, where ordinary dark features accidentally located near bright features are more depressed than those in the slowly varying background. The reduction method of the Stokes I/V filtergrams was a standard one (fg_prep.pro in ssw).

3.2. Hida/DST

For analyzing spectrograms of Ca II H with DST, we first normalized the intensity at the far wing of Ca II H line to compensate for both the temporal variation of the sky transparency and the intensity fluctuation due to granulation (see the left image and panel of figure 4). The intensity normalization was performed to make the average intensities at two wavelengths of Ca II H -3.5 Å and $+3.0$ Å to be constant along the slit and for all time series of the spectral data, since the chromospheric features will not influence the intensities at these far wing wavelengths. Ca II H line profiles of EBs have a double peak. We refer to the blue peak as H_{2V}, and to the red peak as H_{2R}. We then subtracted the intensity profile of quiet regions from those of the EB, and obtained the line-profile features of the EB enhancement (the right image in figure 4). The quiet region intensity profiles were determined for every spatial scan as the average profile of regions of about 2.″6 × 5.″6 far from the active region where there were virtually no magnetic field and no Ca II H bright points. The average intensity profile of the quiet region is also shown by a dashed curve in the lower-left panel of figure 4. The enhancement profile shows a blue asymmetry [$I(H_{2V}) > I(H_{2R})$] in the peak intensities in this figure. We used two measures to estimate the asymmetry of the profile, (1) comparing $I(H_{2V})$ at a given wavelength (3968.36 Å) with $I(H_{2R})$ at another given wavelength (3968.61 Å), and (2) comparing $I(H_{2V})$ of the violet peak and $I(H_{2R})$ of the red peak. The lower-right panel of figure 4 shows the two methods of the analysis, the white circle shows the method of intensity at the given wavelength, and the black circle shows the method of the peak intensity. These two methods nearly show the same results, as will be shown later in figures 9, 12, and 15.

4. Results

Table 1 summarizes the analyses we conducted for each of the EBs. First, we show our results of analysis for all EBs found and listed one by one.

4.1. Individual Ellerman Bomb

4.1.1. Ellerman bomb (A)

EB(A) already existed at the start of our observation, 22:05 UT on 2007 August 9 in Hinode/SOT Ca II H, and lasted about 40 min. In the following, we concentrate on the short-lived behavior of the internal fine structure of the EBs, the brightness enhancement of which was above the 5% of the background intensity. Figure 5 shows the temporal variation of EB(A) images processed by the unsharp masking procedure. The bright and highly elliptical fine structures are seen in the figure as indicated by arrows. It seems that the EB consisted of three bright subcomponents at 22:30:33. We determined the subcomponent that satisfied the following conditions: (1) The brightness enhancement was above 5% of the background intensity, which was determined locally over 1.″1 square area from the smoothed intensity distribution derived by the unsharp masking method. (2) The feature was separated from the others in unsharp masked images. We identified the subcomponents by our eyes, if they showed intensity ridge structures separated from each other. (3) The feature was identified at least in 2 consecutive frames of Hinode/SOT Ca II H images (i.e., longer lifetime than 45 s). (4) The brightness fluctuations of subcomponents were sometimes detected. In this case, the subcomponents were thought to keep alive

Table 1. Times of the observation of four EBs.

EB	Day	(1) Fine structure	(2) Magnetic field	(3) Ca II H spectrum
(A)	2007 Aug 9	22:05–22:38	No data	22:16–22:30
(B)	2007 Aug 9	22:05–22:24	22:05–22:24	22:16–22:21
(C)	2007 Aug 9	22:05–22:33	22:05–22:33	22:16–22:30
(D)	2007 Aug 10	00:28–00:42	00:28–00:42	No data

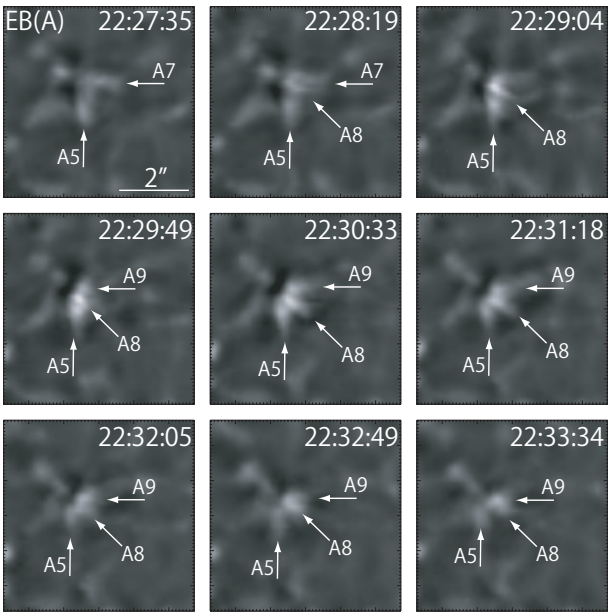

Fig. 5. Time series of EB(A) in Ca II H with SOT. The images were processed by the unsharp masking procedure.

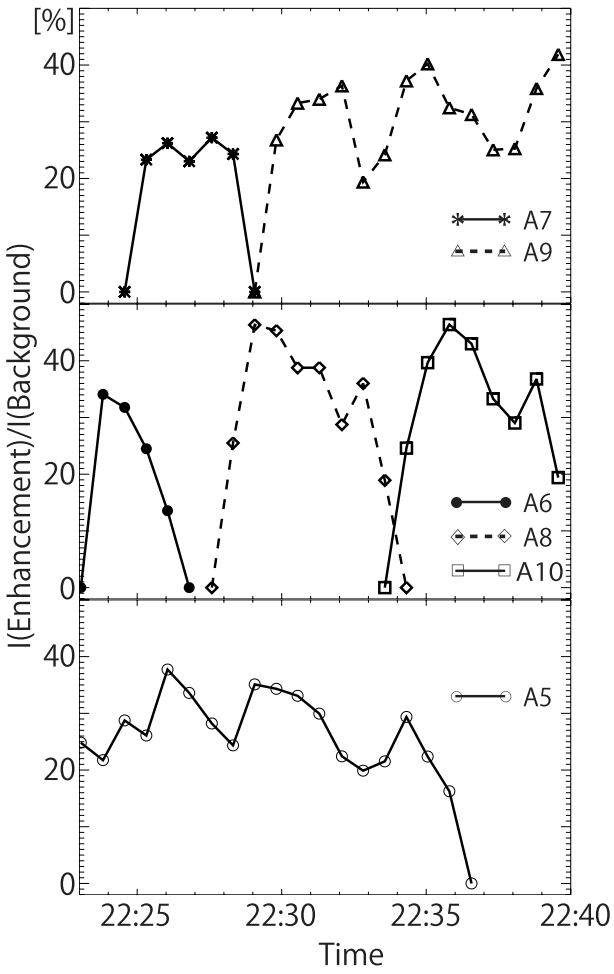

Fig. 6. Temporal variation of the brightness enhancement of the subcomponents detected during 22:13–22:40 UT in the EB(A). Brightness enhancements over their background brightness were plotted in percent values along with the time.

until the time when the brightness went down below the 5% level. Also in (5), on the other hand, there were cases where a new feature started to appear from a pre-existent subcomponent, with a different morphological shape, or with a different direction of elongation from the pre-existent one. We identified this case as the start of a new subcomponent. Figure 6 shows the temporal variation of the brightness enhancement of each subcomponent. As shown in this figure, these subcomponents come up intermittently one by one, spatially juxtaposed to each other. Long durative subcomponents (A5, A9) may be due to a contiguous coming-up of several neighboring subcomponents of much shorter lifetimes.

We also obtained Ca II H spectrograms by scanning the whole region with Hida/DST from 22:16:31 UT to 22:21:16 UT and from 22:24:21 UT to 22:29:03 UT on 2007 August 9. Twenty spectrograms were obtained in total at each spatial position during one series of observation. Figure 7 shows the temporal evolution of Ca II H spectra of EB(A) during a 268 s time span. The cadence was about 15 s. Each spectrum showed the characteristic Ca II H spectra of the EB: a broad emission profile with central absorption. The right panel shows the temporal variation of the Ca II H spectral profile of the EB at different times.

Figure 8 shows the temporal evolution of the EB enhancement spectra from that for the quiet region. The right panel clearly shows the interesting features that the line profile changed from red asymmetry [$I(\mathrm{H_{2V}}) < I(\mathrm{H_{2R}})$] to blue asymmetry [$I(\mathrm{H_{2V}}) > I(\mathrm{H_{2R}})$], or in reverse.

Figure 9 shows the temporal variation of the asymmetry $I(\mathrm{H_{2V}})/I(\mathrm{H_{2R}})$, the integrated intensity from -1.5 Å to $+1.5$ Å around the Ca II H center derived from the spectra taken with DST and the brightness enhancement of each subcomponent identified by Hinode images. The left panels are for the data from 22:16:31 UT to 22:21:16 UT, and the right for those from 22:24:21 UT to 22:29:03 UT. The vertical dash-dotted lines show the observation time of Hinode/SOT. In this figure, we have overlaid the lines that show the trend of the

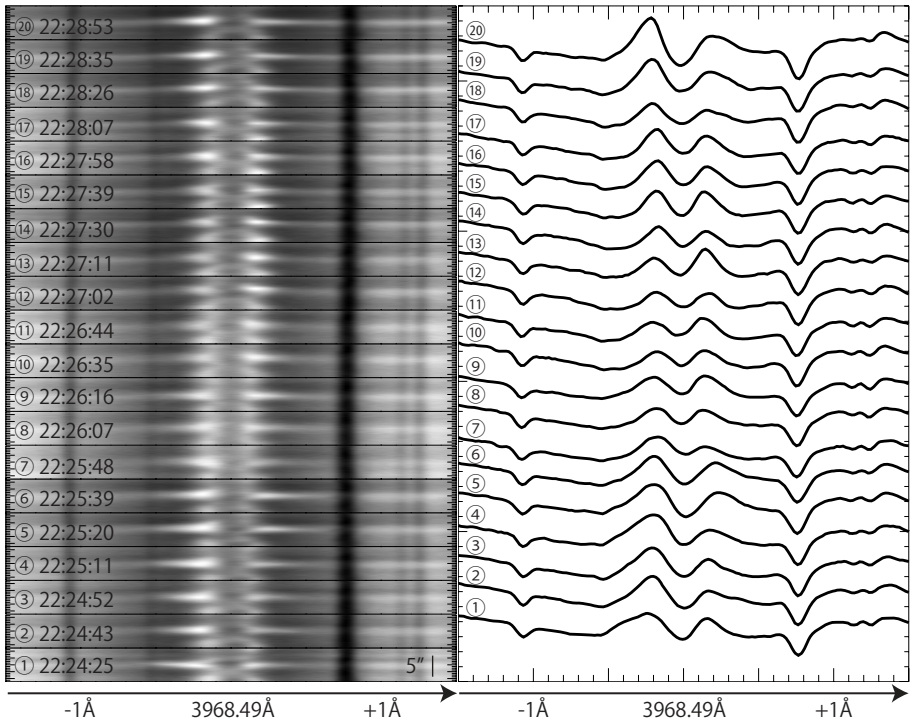

Fig. 7. Temporal evolution of Ca II H spectrograms of EB(A) with Hida/DST. The left images are the Ca II H spectral variation of the EB at twenty different times. The cadence was about 15 s. The right panel is the plots of the Ca II H spectral profiles of the EB at different times. The intensity were normalized ones.

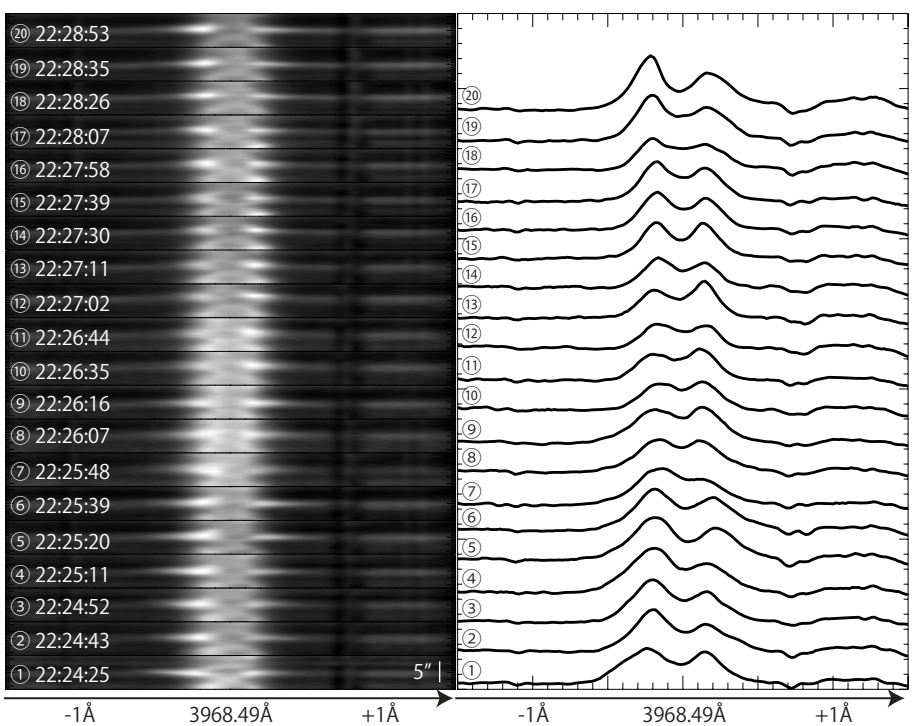

Fig. 8. Temporal evolution of a Ca II H spectral enhancement of EB(A) from those of the quiet regions with Hida/DST. The position and time are the same as in figure 7.

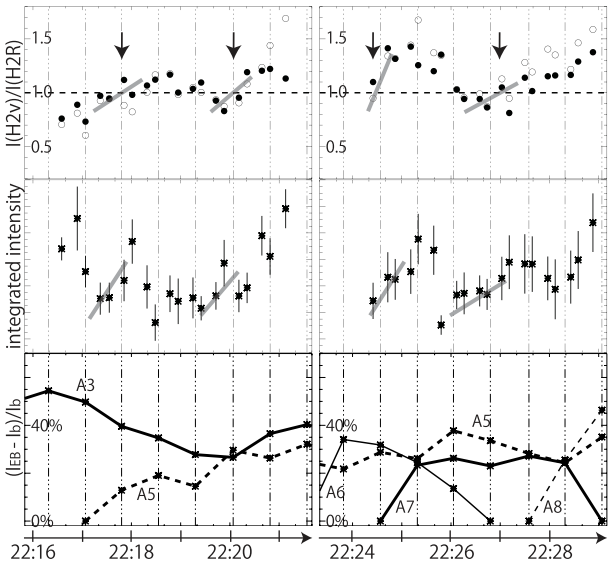

Fig. 9. Temporal variation of $I(\mathrm{H_{2V}})/I(\mathrm{H_{2R}})$ (upper panels), integrated intensity (middle panels) of EB(A), and the brightness enhancement of each subcomponent (lower panels). The left panels are for the data from 22:16:31 UT to 22:21:16 UT and the right were for those from 22:24:21 UT to 22:29:03 UT. The vertical dash-dotted lines show the observation time of Hinode/SOT. The thick arrows indicate the times when the asymmetry of the Ca II H profile changed from red to blue.

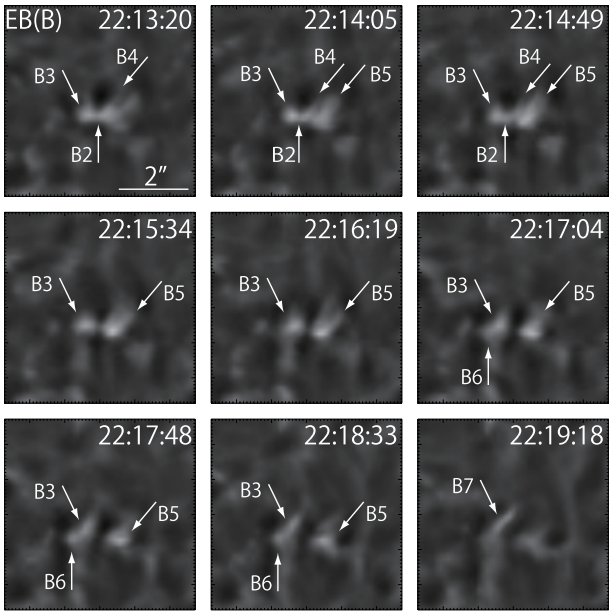

Fig. 10. Time series of EB(B) in Ca II H with SOT. The images were enhanced by the unsharp masking procedure.

variation. The upper-left panel shows that the line profile of the EB changed from red asymmetry to blue asymmetry at 22:17:50 UT and at 22:20:05 UT, and at nearly the same times, the intensity increased, as can be seen from the middle-left panel. The intensity enhancements led to an asymmetry change by 20–40 s. The right panel shows another example of asymmetry change at 22:27:00 UT. The intensity enhancement led to an asymmetry change by 60 s. We can see another less-clear example at around 22:24:20 UT. On the other hand, there is a tendency that the blue asymmetry changes to red in the declining phase of the intensity of EB.

At around the time of the asymmetry change (22:17:50 UT), a subcomponent (A5) identified in the Hinode Ca II H image sequence started to appear (22:17:48 UT). The asymmetry change at 22:20:05 UT corresponds to the re-brightening of A3 (start time: 22:20:04 UT) or to that of A5 (start time: 22:19:18 UT). The right panels also show that the asymmetry change at 22:24:20 UT corresponds to the re-brightening of A5 (start time: 22:23:49 UT) or the appearance of A6 (22:23:29 UT). The asymmetry change at 22:27:00 UT corresponds to the re-brightening of A5 (start time: 22:25:19 UT), or the appearance of A7 (22:25:19 UT). From these examples, we can think that the asymmetry change is associated with the appearance or re-brightening of the subcomponent. The brightness variation seems to lead to the asymmetry change. The brightening of subcomponent A8 has no counterpart of asymmetry change, but seems to correspond to a strengthening of the asymmetry. Successive occurrences of subcomponents may explain this behavior.

4.1.2. Ellerman bomb (B)

EB(B) also already existed at 22:05 UT on 2007 August 9 in Hinode/SOT Ca II H, and lasted about 20 min. We analyzed the EB by the same method as for EB(A). Figure 10 shows the time series of the processed images of the EB observed in Ca II H with SOT. In the figure, we can see two bright and highly elliptical fine structures at 22:13:20 UT. They changed their morphological shapes, temporally.

We also obtained the data of Stokes V of EB(B). Figure 11 shows the time series of the EB observed in Ca II H and Stokes V with SOT. The left images are the data of Ca II H with SOT with contour lines. Also, the right images are maps of the Stokes V with Ca II H contour lines. The blue and red color regions show negative and positive polarities. These images show that the subcomponents started to appear on the magnetic neutral lines, and extended their lengths from the original locations. Also, in the lower 2 images of Stokes V, the regions of positive polarity eventually came to vanish.

We also obtained spectrograms of Ca II H with Hida/DST from at 22:16:31 UT to at 22:21:16 UT on 2007 August 9. Figure 12 shows the temporal variation of $I(\mathrm{H_{2V}})/I(\mathrm{H_{2R}})$, the integrated intensity of the EB, and the brightness enhancement of each subcomponent. The upper panel shows that the line profile of the EB changed from red asymmetry to the blue at 22:19:00 UT, and at the same time, the intensity increased, as can be seen from the middle panel. This correlation also can be interpreted by being a weakening of one subcomponent and the brightening of another subcomponent, because at around the time of the asymmetry change, a subcomponent (B7) identified in the Hinode Ca II H image sequence started to appear (22:19:18 UT). On the other hand, we can not see the corresponding asymmetry change to the appearance of B6. Since the spatial resolution of DST spectroscopy is inferior to that of Hinode, the spectral characteristics derived by DST reflect those of the co-existent brighter subcomponents in the EB. A less-bright subcomponent cannot contribute to the spectral features of a spatially mixed subcomponents in the EB.

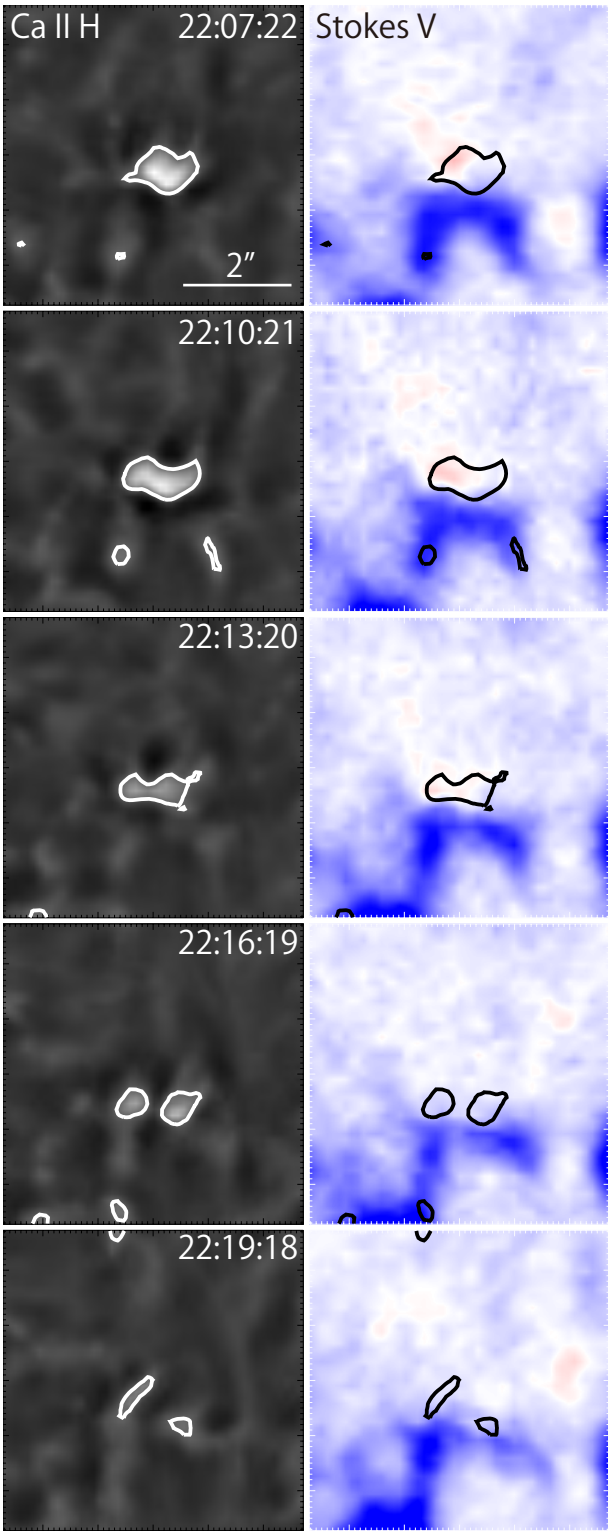

Fig. 11. Time series of EB(B) observed in Ca II H and Stokes V with SOT. The left images are the data of Ca II H with SOT processed by the unsharp masking procedure with contour lines. And the right images are the data of Stokes V with Ca II H contour lines. The blue and red color regions show negative and positive polarities.

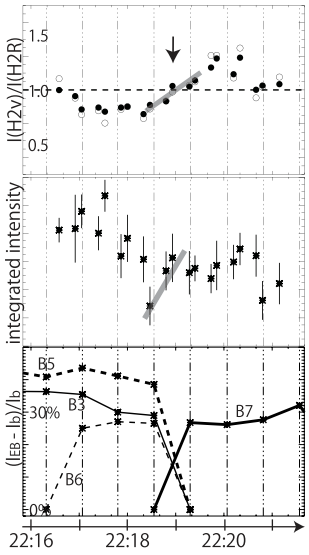

Fig. 12. Temporal variation of $I(\mathrm{H_{2V}})/I(\mathrm{H_{2R}})$ (upper panel), integrated intensity (middle panel) of EB(B), and the brightness enhancement of each subcomponent (lower panels). These panels are for the data from 22:16:31 UT to 22:21:16 UT. The vertical dashed lines show the observation time of Hinode/SOT. The thick arrows indicates the times when the asymmetry of the Ca II H profile changed from red to blue.

4.1.3. Ellerman bomb (C)

EB(C) also already existed at 22:05 UT on 2007 August 9 in Hinode/SOT Ca II H, and lasted for about 30 min. We analyzed the EB by the same method as for EB(A). Figure 13 shows the time series of the processed images of the EB observed in Ca II H with SOT. In the figure, we can see some bright subcomponents. They changed their brightness temporally and moved spatially in the south-west direction.

Figure 14 shows the time series of the EB observed in Ca II H and Stokes V with SOT. The blue and red color regions of the right images show negative and positive polarities. The EB was on the neutral line, and overstride both polarities.

We also obtained spectrograms of Ca II H with Hida/DST from 22:16:31 UT to 22:21:16 UT and from 22:24:21 UT to 22:29:03 UT on 2007 August 9. Figure 15 shows the temporal variation of $I(\mathrm{H_{2V}})/I(\mathrm{H_{2R}})$, the integrated intensity of the EB, and the brightness enhancement of each subcomponent. The upper-left panel shows that the line profile of the EB changed from red asymmetry to blue asymmetry at 22:19:00 UT. Also, at 22:18:30 UT, the intensity started to increase, as can be seen from the middle-left panel. The intensity enhancement leads to an asymmetry change by 30 s. The upper-right panel shows the blue asymmetry of the line profile of the EB become strong again at 22:25:40 UT, also, at nearly the same time, the intensity increased, as can be seen from the middle-right panel. At around the times of asymmetry change (22:19:00 UT and 22:25:40 UT), subcomponents (C3 and C5) identified in Hinode Ca II H image sequence started to appear (22:19:18 UT and 22:26:03 UT). This correlation supports our view that when the intensity of a subcomponent started to increase, the EB showed blue asymmetry.

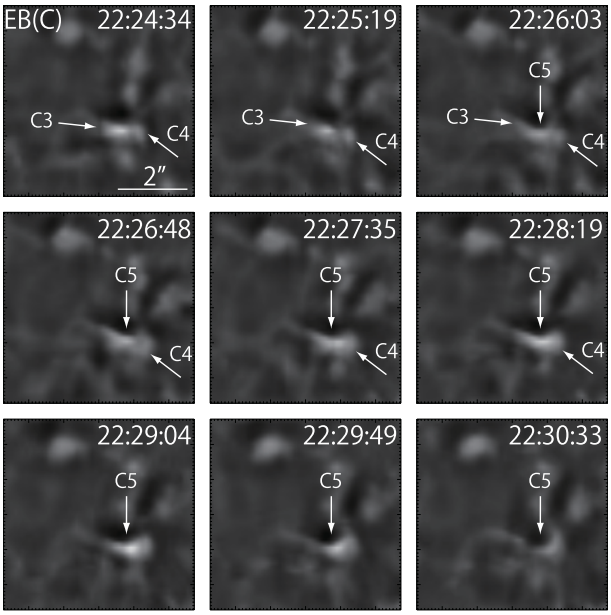

Fig. 13. Time series of EB(C) in Ca II H with SOT. The images were processed by the unsharp masking procedure.

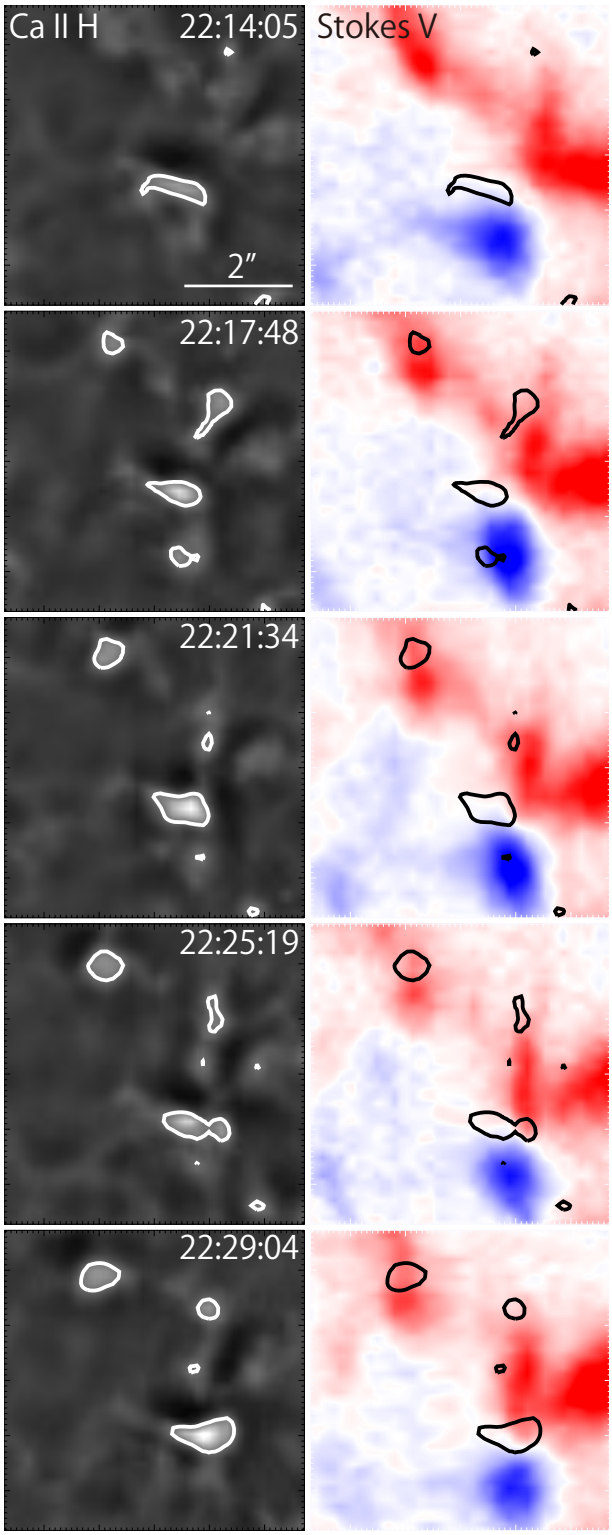

Fig. 14. Time series of EB(C) observed in Ca II H and Stokes V with SOT. The left images are the data of Ca II H with SOT processed by the unsharp masking procedure with contour lines. And the right images are the data of Stokes V with Ca II H contour lines. The blue and red color regions show negative and positive polarities.

4.1.4. *Ellerman bomb (D)*

EB(D) emerged at 00:30 UT on 2007 August 10 in Hinode/SOT Ca II H, and lasted for about 10 min. We analyzed the EB by the same method as for EB(A). Figure 16 shows the time series of the processed images of the EB observed in Ca II H with SOT. In this figure, we can see the existence of some bright subcomponents and spatial movement to the north.

Figure 17 shows the time series of the EB observed in Ca II H and Stokes V with SOT. The blue and red color regions of the right images show negative and positive polarities. These images show that the positive polarity was emerging, and after that the positive polarity of the EB disappeared. We thus think the reconnection between the emerging flux region and the preexistent negative polarities happened during this event.

4.2. *Fine Structure of Ellerman Bomb*

As mentioned in the previous section, we found that the EBs consisted of several subcomponents in Ca II H images of SOT (figures 5, 10, 13, 16). Table 2 is a summary of our measurements of the duration, width, length, aspect ratio of each subcomponent, and figure 18 is their histograms. The mean duration, the mean width, the mean length, the mean aspect ratio of the subcomponents were 390 s, 170 km, 450 km and 2.7, respectively. The aspect ratio of the EB subcomponents is 2.7, while those of the EBs themselves are around 1.5 (1400 km/980 km), as derived by Pariat et al. (2007). Thus, the subcomponents of the EBs have more eccentric geometrical shapes, which suggest a jet-like or loop-like formation of the subcomponents, EB(A), as an entity shows spatial movement during its life, while the subcomponents did not show any movements. We thus think that the spatial movements of the EBs are due to a successive coming-up of the subcomponents.

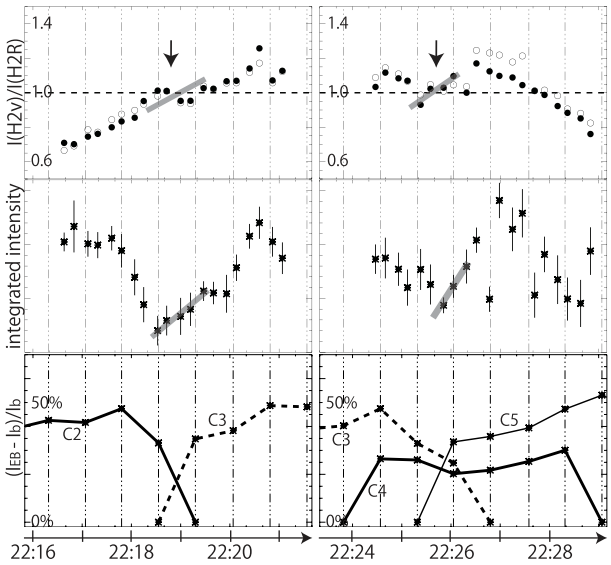

Fig. 15. Temporal variation of $I(\mathrm{H_{2V}})/I(\mathrm{H_{2R}})$ (upper panels), integrated intensity (middle panels) of EB(C), and the brightness enhancement of each subcomponent (lower panels). The left panels are for the data from 22:16:31 UT to 22:21:16 UT and the right are for those from 22:24:21 UT to 22:29:03 UT. The vertical dashed lines show the observation time of Hinode/SOT. The thick arrows indicate the times when the asymmetry of the Ca II H profile changed from red to blue.

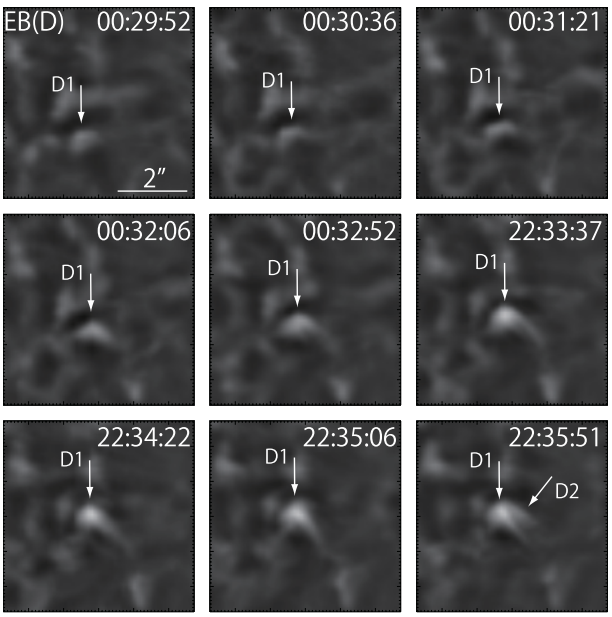

Fig. 16. Time series of EB(D) in Ca II H with SOT. The images were processed by the unsharp masking procedure.

The spectroscopic asymmetry changes are associated with a new appearance or re-brightening of the subcomponents. Also, it seems highly probable that the activity of the subcomponents gives rise to the blue asymmetry, as analyzed in the previous subsections.

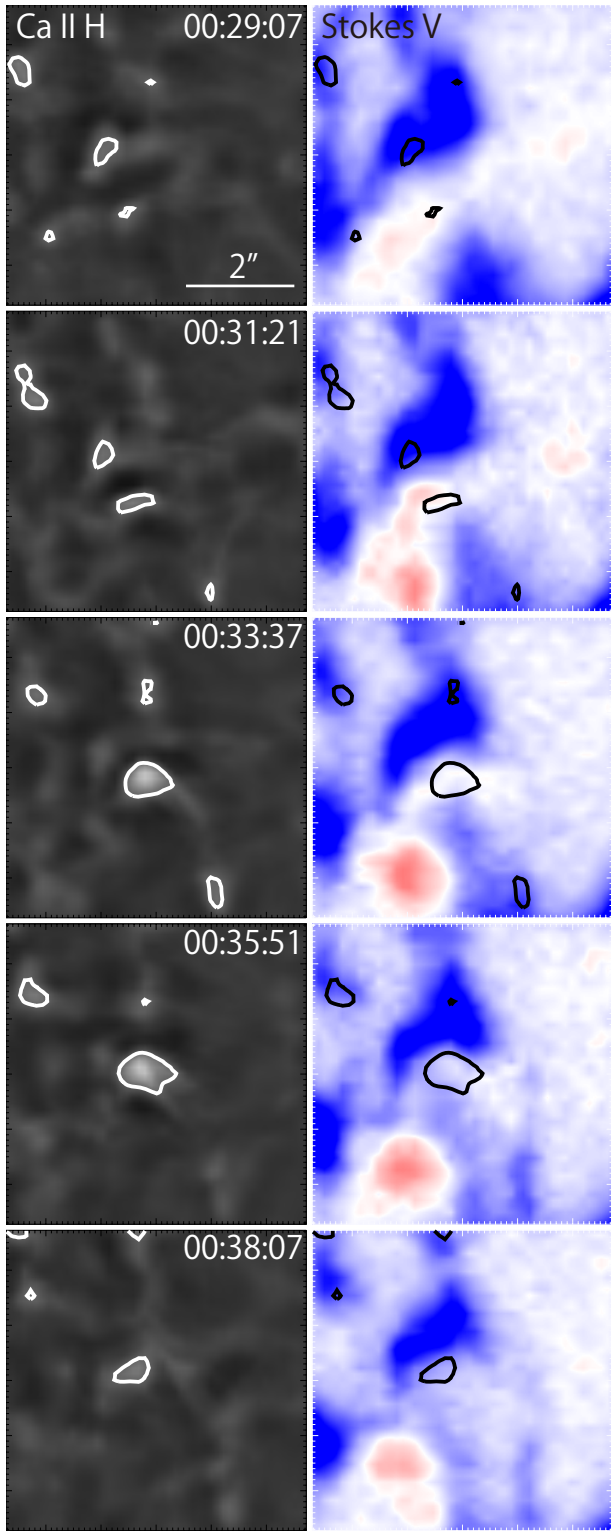

Fig. 17. Time series of EB(D) observed in Ca II H and Stokes V with SOT. The left images are the data of Ca II H with SOT processed by the unsharp masking procedure with contour lines. And the right images are the data of Stokes V with Ca II H contour lines. The blue and red color regions show negative and positive polarities.

Table 2. Characteristics of subcomponents of the EBs.

EB	No.	Start	End	T [s]	W [km]	L [km]	Aspect ratio [L/W]
(A)	1	—	22:08:07	—	183	351	1.9
	2	22:08:52	22:17:48	536	92	320	3.5
	3	22:09:36	22:23:49	853	122	260	2.1
	4	22:12:35	22:16:19	224	179	375	2.1
	5	22:17:48	22:35:48	1080	183	416	2.3
	6	22:23:49	22:26:03	134	183	214	1.2
	7	22:25:19	22:28:19	180	107	385	3.6
	8	22:28:19	22:33:34	315	140	491	3.5
	9	22:29:49	22:43:19	810	167	457	2.7
	10	22:34:19	22:39:33	314	165	706	4.3
	11	22:41:49	22:47:04	315	215	399	1.9
(B)	1	—	22:12:35	—	183	213	1.2
	2	—	22:14:49	—	141	513	3.6
	3	22:09:36	22:18:33	537	159	453	2.8
	4	22:11:50	22:14:49	179	153	543	3.5
	5	22:14:05	22:18:33	268	194	561	2.9
	6	22:17:04	22:18:33	89	153	229	1.5
	7	22:19:18	22:22:18	180	195	758	3.9
(C)	1	—	22:09:36	—	178	669	3.8
	2	22:08:52	22:18:33	581	137	492	3.6
	3	22:19:18	22:26:03	405	214	430	2.0
	4	22:24:34	22:28:19	225	201	391	1.9
	5	22:26:03	22:30:33	270	168	275	1.6
(D)	1	00:29:07	00:36:36	659	248	755	3.0
	2	00:35:51	00:38:07	136	173	580	3.4

* T: duration, W: width, and L: length.

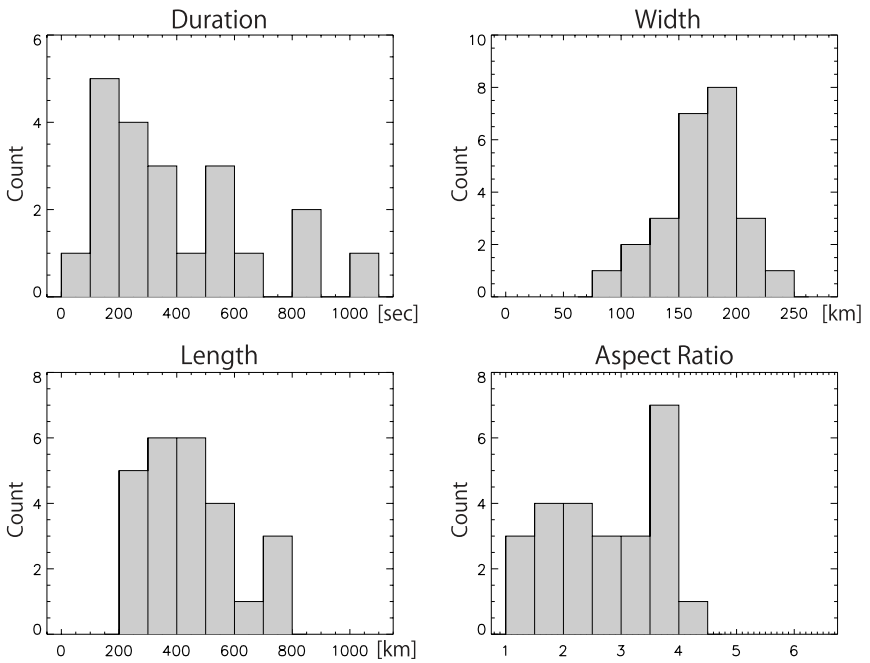

Fig. 18. Histograms of the duration, width, length, aspect ratio of subcomponents.

5. Summary & Discussion

We observed EBs that appeared in NOAA 10966 with Hinode/SOT and Hida/DST. From this study, the following properties about EBs were found:

(a) The EBs were composed of a few of fine subcomponents. The mean duration, the mean width, the mean length, the mean aspect ratio of the subcomponents were 390 s, 170 km, 450 km, and 2.7, respectively.
(b) Subcomponents started to appear on the magnetic neutral lines, and extended their lengths from the original locations.
(c) When Ca II H line of EBs showed the characteristic blue asymmetry, they are associated with the appearance or re-brightening of a subcomponent. On the other hand, the asymmetry showed a tendency to change to the red when the subcomponents decayed.

A previous study showed that the typical size of EBs is on the order of 1″ (700 km), and the typical lifetime is 10–20 min. Roy and Leparskas (1973) showed that the mean duration of EBs at H$\alpha-2$ Å was about 13 min near the disk center, and Kurokawa et al. (1982) showed that the mean duration at H$\alpha-1.2$ Å was about 12 min, the mean length was 1.″1 (770 km), and the width was less than 0.″6 (420 km), and Pariat et al. (2007) showed that the mean width was 1.″4 (980 km) and the mean length was 2.″0 (1400 km) at Ca II 8542 Å. We observed at Ca II H, and have newly found the subcomponents of EBs, and the duration of the subcomponents were shorter than the typical lifetime of EBs, and smaller than the typical size of EBs. As can be seen in figure 8, the emission profiles of the EBs change their width along with the time of evolution. The lifetimes of EBs determined in the very far wing generally are shorter than those determined in inner wing wavelengths. SOT BFI imager detected enhancements in the 3 Å passband. So we expect that the lifetimes derived with the SOT Ca II H images will be longer than the previous monochromatic observations in the far wings. In spite of this expectation, we obtained shorter lifetimes than in the previous studies. Thus, we think that the longer lifetime and larger size of EBs thus far obtained resulted from the consecutive coming-up of the short-lived subcomponents.

The initial location of the subcomponents was on the magnetic neutral lines. Kitai (1983) suggested that heating the lower chromosphere plays an important role in producing the characteristic line profiles of EBs. Thus, the chromospheric magnetic reconnection will be the trigger and the driver of EBs. We think that the blue asymmetric Ca II H profile is due to the upward-moving jets. The association of the blue asymmetry and the brightening of Ca II H spectra is evidence of our interpretation. Figure 19a is the most generally accepted view of the triggering models for EBs, i.e., the magnetic reconnection model in inverse Ω-shaped magnetic field (Pariat et al. 2004; Matsumoto et al. 2008b; Watanabe et al. 2008). Pariat et al. (2004) observed that EBs are linked by a hierarchy of elongated flux tubes showing aperiodic spatial undulations, and EBs occur as a result of magnetic reconnection at the dipped lower parts. Matsumoto et al. (2008b) and Watanabe et al. (2008) observationally supported the model. However, all previous observations were made for EBs occurring in actively developing emerging flux regions. The EBs studied in the present paper were those occurring in the magnetic cancellation area, or small-scale emerging flux region. In these situations, it seems that another view depicted in figure 19b would be possible to form the magnetic configuration for reconnection. Magnetic reconnection between pre-existent field and moving-in magnetic field of opposite polarity triggers the ejection of a jet-like subcomponent. A numerical simulation study in the corona supported the magnetic reconnection model between an emerging magnetic bipole and a pre-existing uniform field (Yokoyama & Shibata 1995; Nishizuka et al. 2008). In the chromosphere, magnetic reconnection will occur with the same magnetic configuration.

The mechanism to drive EBs is magnetic reconnection, and is common to both scenarios depicted in figures 19a and 19b. The difference between these scenarios is the formation process of the magnetic configuration, which gives rise to magnetic reconnection. One is the resistive emergence of the magnetic flux, and the other is the moving-in magnetic feature to the pre-existing magnetic field.

Next, let us discuss the observational visibility of subcomponents in EBs. Pariat et al. (2007) and Matsumoto et al. (2008b) reported elliptical shapes of EBs. The elliptical shapes of EBs were interpreted as due to the magnetic reconnection in the current sheet of U-shaped magnetic topology. However, the geometrical sizes of EBs studied by them were much larger than the subcomponents of EBs and the aspect ratio of their EBs were also different from those of subcomponents. We thus think that the shapes of EBs will depend upon the magnetic configuration surrounding the EBs (figure 19a or 19b). Subcomponents of EBs will be detected in an active emerging flux region by high spatial and temporal observations in near future, as we expect that magnetic reconnection in the model of figure 19a will also show the intermittency or bursty nature of magnetic reconnection.

Finally, another important fact that we found is that magnetic reconnections do not occur continuously, but intermittently. These elementary reconnections (i.e., subcomponents) come up one by one, spatially juxtaposed to each other. Qiu et al. (2000) and Pariat et al. (2007) from the total intensity variation of EBs in Hα wing and/or in UV (1600 Å), pointed out the rapid fluctuation of EB brightness or successive enhanced emissions. In the present work, we found the actual spatially distinguished subcomponents of EBs, whose intermittent and consecutive coming-up will produce the temporal brightness fluctuations of EBs. Similar behavior of multiple consecutive Hα brightening was often observed at the footpoints of chromospheric surge events (R. Kitai 2009, private communication). Thus, the intermittency may be a common feature of chromospheric magnetic reconnection. A few recent numerical simulation studies of magnetic reconnection in the coronal magnetic field suggested intermittent reconnection (Nishida et al. 2009). The same characteristics may be relevant in chromospheric magnetic reconnection.

In conclusion, chromospheric magnetic reconnection is the trigger and the driver of EBs. According to the magnetic configuration, EBs will occur either by the model of figures 19a or 19b. Magnetic reconnections do not occur continuously, but

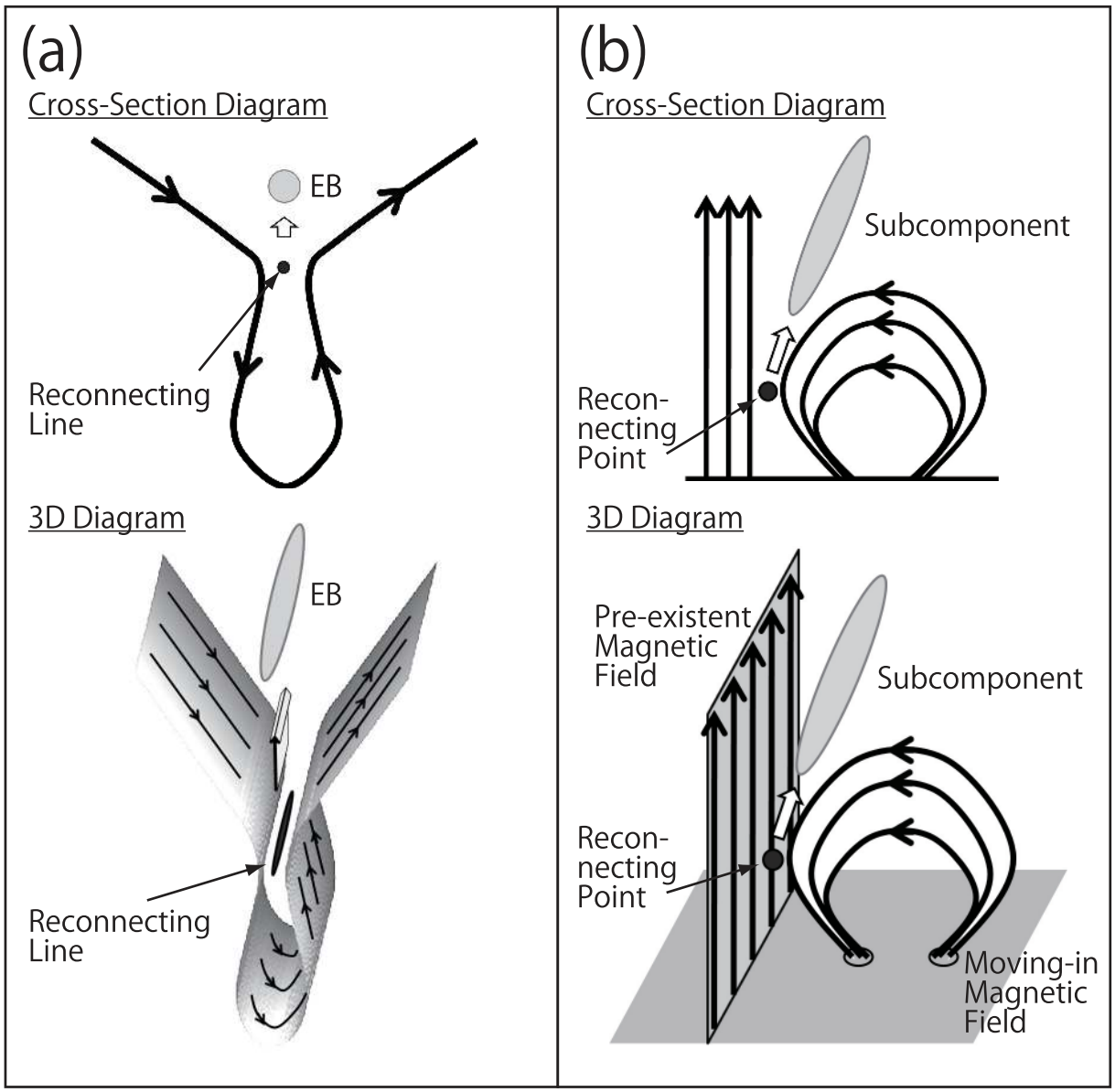

Fig. 19. Triggering models of EBs. (a) The magnetic reconnection model in inverse Ω-shaped magnetic field, which is the most generally accepted one for EBs in emerging flux regions. (b) Magnetic reconnection between pre-existent field and moving-in magnetic field of opposite polarity, which is the case of this paper.

intermittently. Further numerical studies are strongly needed to clarify the physics of chromospheric magnetic reconnection.

We express our gratitude to an anonymous referee whose comments greatly helped us to clarify the contents of the paper. We are grateful to all the staff members of the Kwasan and Hida Observatories, Kyoto University for their guidance of the Domeless Solar Telescope and for the fruitful discussions with them. This work was supported by the Grant-in-Aid for the Global COE Program "The Next Generation of Physics, Spun from Universality and Emergence" from the Ministry of Education, Culture, Sports, Science and Technology (MEXT) of Japan, by the Grant-in-Aid for Creative Scientific Research The Basic Study of Space Weather Prediction (17GS0208, PI: K. Shibata) from the MEXT of Japan, and by the grant-in-aid from the Japanese MEXT (19540474).

References

Ding, M. D., Hénoux, J.-C., & Fang, C. 1998, A&A, 332, 761
Ellerman, F. 1917, ApJ, 46, 298
Firstova, N. M. 1986, Sol. Phys., 103, 11
Georgoulis, M. K., Rust, D. M., Bernasconi, P. N., & Schmieder, B. 2002, ApJ, 575, 506
Hénoux, J.-C., Fang, C., & Ding, M. D. 1998, A&A, 337, 294
Ichimoto, K., et al. 2004, Proc. SPIE, 5487, 1142
Isobe, H., Tripathi, D., & Archontis, V. 2007, ApJ, 657, L53
Kitai, R. 1983, Sol. Phys., 87, 135
Kurokawa, H., Kawaguchi, I., Funakoshi, Y., & Nakai, Y. 1982, Sol. Phys., 79, 77
Malin, D. F. 1977, Am. Astron. Soc. Photogr. Bull., 16, 10
Matsumoto, T., et al. 2008b, PASJ, 60, 577
Matsumoto, T., Kitai, R., Shibata, K., Otsuji, K., Naruse, T., Shiota, D., & Takasaki, H. 2008a, PASJ, 60, 95
Nakai, Y., & Hattori, A. 1985, Memoirs of the Faculty of Science, Kyoto University, Series A of Physics, Astrophysics, Geophysics and Chemistry, 36, 385
Nindos, A., & Zirin, H. 1998, Sol. Phys., 182, 381
Nishida, K., Shimizu, M., Shiota, D., Takasaki, H., Magara, T., & Shibata, K. 2009, ApJ, 690, 748
Nishizuka, N., Shimizu, M., Nakamura, T., Otsuji, K., Okamoto, T. J., Katsukawa, Y., & Shibata, K. 2008, ApJ, 683, L83
Pariat, E., Aulanier, G., Schmieder, B., Georgoulis, M. K., Rust, D. M., & Bernasconi, P. N. 2004, ApJ, 614, 1099
Pariat, E., Schmieder, B., Berlicki, A., Deng, Y., Mein, N., López Ariste, A., & Wang, S. 2007, A&A, 473, 279
Parker, E. N. 1966, ApJ, 145, 811
Qiu, J., Ding, M. D., Wang, H., Denker, C., & Goode, P. R. 2000, ApJ, 544, L157
Roy, J.-R., & Leparskas, H. 1973, Sol. Phys., 30, 449
Shimizu, T., et al. 2008, Sol. Phys., 249, 221
Suematsu, Y., et al. 2008, Sol. Phys., 249, 197
Tsuneta, S., et al. 2008, Sol. Phys., 249, 167
Watanabe, H., et al. 2008, ApJ, 684, 736
Yokoyama, T., & Shibata, K. 1995, Nature, 375, 42
Zachariadis, Th. G., Alissandrakis, C. E., & Banos, G. 1987, Sol. Phys., 108, 227